

Since $V^\mu(\tau)$ is arbitrary, Eq. (A4) is equivalent to the relation

$$\frac{dA^{\mu'}_{\nu'}(\tau)}{d\tau} = - \left\{ \begin{matrix} \mu' \\ \rho'\sigma' \end{matrix} \right\} A^{\rho'}_{\nu'}(\tau) \frac{dx^{\sigma'}}{d\tau}, \quad (\text{A5})$$

which gives the parallel-transported components of $A^{\mu'}_{\nu'}(\tau)$.

The transport tensor may be written in the form

$$T^{\mu'}_{\nu'}(\tau, \tau', \xi) = A^{\mu'}_{\rho'}(\tau, \xi) A^{\rho'}_{\nu'}(\tau', \xi). \quad (\text{A6})$$

We shall assume that the components of $V^{\mu'}(\tau)$ parallel transported from τ' to τ are given by

$$V^{\mu'}(\tau) = T^{\mu'}_{\nu'}(\tau, \tau') V^{\nu'}(\tau') = A^{\mu'}_{\rho'}(\tau) A^{\rho'}_{\nu'}(\tau') V^{\nu'}(\tau'). \quad (\text{A7})$$

Then by differentiation along the path, we obtain

$$\frac{dV^{\mu'}(\tau)}{d\tau} = \frac{dA^{\mu'}_{\rho'}(\tau)}{d\tau} A^{\rho'}_{\nu'}(\tau') V^{\nu'}(\tau'). \quad (\text{A8})$$

Substitute Eq. (A5) into Eq. (A8) and use Eq. (A7) to find the result:

$$\begin{aligned} \frac{dV^{\mu'}(\tau)}{d\tau} &= - \left\{ \begin{matrix} \mu' \\ \rho'\sigma' \end{matrix} \right\} \frac{dx^{\sigma'}}{d\tau} A^{\rho'}_{\lambda'}(\tau) A^{\lambda'}_{\nu'}(\tau') V^{\nu'}(\tau') \\ &= - \left\{ \begin{matrix} \mu' \\ \rho'\sigma' \end{matrix} \right\} \frac{dx^{\sigma'}}{d\tau} V^{\rho'}(\tau). \end{aligned} \quad (\text{A9})$$

Thus $V^{\mu'}(\tau)$ as defined by Eq. (A7) satisfies the equation of parallel transport. We must conclude that the transport tensor provides us with the parallel-transported components of any vector if we have the components at some point on the path. This result is obvious if we look at Eq. (A7) in the inertial frame

$$V^\mu(\tau) = V^\mu(\tau'). \quad (\text{A7}')$$

Experimental Test of the Pion-Nucleon Forward Dispersion Relations at High Energies*

K. J. FOLEY, R. S. JONES,† S. J. LINDENBAUM, W. A. LOVE, S. OZAKI, E. D. PLATNER, C. A. QUARLES,‡ AND E. H. WILLEN

Brookhaven National Laboratory, Upton, New York 11973

(Received 2 December 1968)

The small-angle differential scattering cross sections of protons for pions have been measured to high precision at the Brookhaven AGS. The range of incident momenta was 8–20 GeV/c for π^+ , and 8–26 GeV/c for π^- . The real part of the pion-nucleon forward scattering amplitude was determined by observing its interference with the known Coulomb amplitude. Combining these results with precision measurements of pion-proton total cross sections over this energy range provided a critical test of the predictions of the forward dispersion relations. The results demonstrate the validity of the dispersion relations up to at least 20 GeV/c laboratory momentum. The predictions of charge independence are also verified by comparing these experimental measurements with forward charge-exchange scattering cross sections. Furthermore, if microscopic causality is violated, this occurs at “distances” less than 10^{-18} cm.

I. INTRODUCTION

THE purpose of this experiment was to test the pion-nucleon forward dispersion relations at high energy by measuring the real part of the pion-nucleon forward scattering amplitude. The real part was measured by observing the Coulomb-nuclear interference in pion-nucleon differential elastic scattering in the angular range 0–22 mrad at incident laboratory momenta from 8–26 GeV/c for π^-p and 8–20 GeV/c for π^+p . These energies are sufficiently high that the dispersion-relation predictions are very insensitive to uncertainties in the low-energy parameters and the

range of energies is large enough that we can perform sufficient subtractions to remove the dependence on the asymptotic behavior of the total cross sections. As a separate part of the experiment, we measured total cross sections in this energy region with an absolute precision of 0.3%.¹ This enabled us to evaluate the dispersion-relation integrals more precisely and also improved the determination of the real part of the scattering amplitude.

An earlier incomplete investigation² had established that there were sizable real parts of the pion-nucleon forward scattering amplitude at high energy. However,

* Work performed under the auspices of the U. S. Atomic Energy Commission.

† Present address: University of Minnesota, Minneapolis, Minn.

‡ Present address: Texas Christian University, Fort Worth, Tex.

¹ K. J. Foley, R. S. Jones, S. J. Lindenbaum, W. A. Love, S. Ozaki, E. D. Platner, C. A. Quarles, and E. H. Willen, *Phys. Rev. Letters* **19**, 330 (1967).

² K. J. Foley, R. S. Gilmore, R. S. Jones, S. J. Lindenbaum, W. A. Love, S. Ozaki, E. H. Willen, R. Yamada, and L. C. L. Yuan, *Phys. Rev. Letters* **14**, 862 (1965).

the large systematic uncertainty in the real parts deduced from that experiment prevented a conclusive test of the forward dispersion relations. Since the data presented herein have much higher precision and cover a wider energy range, they should supersede the earlier results.² Previous isolated measurements³ for π^-p at 3.5 and 6.4 GeV/*c* were consistent with the dispersion-relation predictions but had large errors ($\sim 30\%$). At energies up to a few hundred MeV, the forward amplitudes deduced indirectly from phase-shift analysis are in agreement with the dispersion-relation predictions.⁴ However, in all of these cases the uncertainties in the experiments and their analysis, low-energy parameters, and asymptotic behavior were sufficiently large to prevent a critical test of the forward dispersion relations.

The results given here have been presented previously in preliminary form.⁵

II. APPARATUS

The experimental layout at the Brookhaven Alternating Gradient Synchrotron (AGS) is shown in Fig. 1. The momentum-separated pion beam incident on the liquid-hydrogen target was defined by the scintillation counters S1, S2, the ring anticoincidence counters A1, A2, A3, the threshold Cherenkov counters CT1, CT2, and the scintillation-counter hodoscopes H01, H02. The hodoscopes were used to measure the incident angle with an accuracy of ± 0.13 mrad. Scattering angles and momenta were measured by H01, H02, H2, and H4. (The number of elements in the hodoscopes and their dimensions are given in Table I, together with the distance of each screen from H01.) Three bending magnets, each with a gap 30-in. wide by 72-in. long by 6-in. high, were used as analyzing magnets to separate elastic scattering interactions. They were adjusted at each momentum to bend the unscattered beam through 6° . The geometric resolutions were ± 0.2 and ± 0.3 mrad for the 0.127- and 0.266-in.-wide counters in H2, respectively; the spread due to multiple scattering varied from 0.5 mrad at 8 GeV/*c* to 0.2 mrad at 26

GeV/*c*. The momentum resolution (rms) including the beam-momentum spread, varied from 0.46% at 8 GeV/*c* to 0.27% at 26 GeV/*c*, being partially limited by multiple scattering. The hodoscopes H1X and H1Y were used together with the other screens to locate the position of interaction and thus to reject scattering from regions outside the liquid-hydrogen target. In order to reduce background interactions and multiple scattering, the regions H01 to H02, H02 to the hydrogen target, and the hydrogen target to H1 contained evacuated pipes, while the regions H1 to H2 and H2 to H4 were filled with helium bags. The PDP-6 computer system of the Brookhaven On-Line Data Facility was used for on-line reconstruction of the scattering events, for monitoring of the experiment, and for feedback of the results in real time.

The need to measure both π^+p and π^-p scattering up to the highest possible energy with the same apparatus dictated the beam design. The negative beam was produced at zero degrees from a 0.5-in.-long 0.04-in.-diam Be wire target in the F9 straight section of the AGS. It was bent by the F9 AGS ring magnet on to the same line as the positive beam, which was produced at 4.5° from a similar Be wire target in the F10 straight section and deflected only slightly by the fringing field of the F10 magnet. The beam transport was made up of two quadrupole doublets to focus the beam on the liquid-hydrogen target, plus three 18D72 bending magnets to provide momentum separation.

At energies up to 20 GeV/*c* the π^- beam contained 5×10^4 particles per pulse and was controlled by changing the number of primary protons striking the AGS target. Above 20 GeV/*c*, the beam rate fell off with increasing energy to 1.5×10^4 pions/pulse at 26 GeV/*c*. The π^+ beam rate varied from 5×10^4 pions/pulse at 8 GeV/*c* to 10^8 pions/pulse at 20 GeV/*c*. The debunched flat-top spill was typically 400-msec long. Vacuum pipes or He bags were used along the full length of the beam to reduce multiple scattering.

TABLE I. Physical dimensions of the hodoscope counters. The narrower counters in the H1X and H2X screens were located at the end through which the unscattered beam passed in order to have better resolution at the smaller scattering angles. Distances between the hodoscopes are also shown.

Hodoscope	Number of elements	Dimensions (in.)			Distance from H01 (in.)
		width	length	thickness	
H01X	12	0.123	1.5	0.125	0
H01Y	12	0.123	1.5	0.125	0
H02X	10	0.123	1.25	0.0625	951.4
H02Y	10	0.123	1.25	0.0625	951.4
H1X	24	0.126	4.0	0.125	1504.4
H1Y	32	0.126	4.0	0.125	1531.4
H2X	48	0.127	6.0	0.30	1991.4
H2Y	80	0.266	6.0	0.30	1991.4
H4X	120	0.504	12.0	0.50	3560.9
H4Y	24	0.500	60.0	0.50	3560.9
Center of liquid-hydrogen target					1220.9

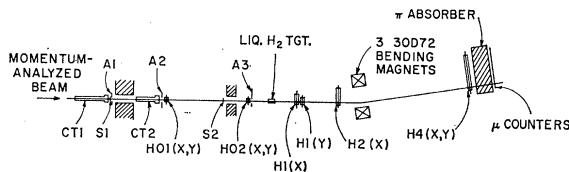


FIG. 1. Experimental arrangement. Distances of the hodoscopes along the beam are approximately to scale. Precise values of the positions are given in Table I.

³ A. A. Nomofilov, I. M. Sitnik, L. A. Slepets, L. P. Strunov, and L. S. Zolin, Zh. Eksperim. i Teor. Fiz. Pis'ma v Redaktsiyu **6**, 546 (1967) [English transl.: Soviet Phys.—JETP Letters **6**, 65 (1967)].

⁴ J. Hamilton and W. S. Woolcock, Rev. Mod. Phys. **35**, 737 (1963).

⁵ K. J. Foley, R. S. Jones, S. J. Lindenbaum, W. A. Love, S. Ozaki, E. D. Platner, C. A. Quarles, and E. H. Willen, Phys. Rev. Letters **19**, 193 (1967).

Pions were selected by two 15-ft-long air-filled threshold Cherenkov counters, CT1 and CT2, used in coincidence. The pressure chosen for these Cherenkov counters varied from 1 atm at 8 GeV/c to $\frac{1}{3}$ atm at 26 GeV/c. The proton contamination of the π^+ beam was measured to be less than 0.03% at both high and low momentum by placing a gas-differential Cherenkov counter⁶ in the beam downstream of the threshold counters during test periods. Kaon contamination and antiproton contamination were negligible in all cases. A 40-ft-long threshold Cherenkov counter set below the muon threshold was used to determine that the electron contamination of the beam was less than 0.1% at 10 GeV/c. Since the γ -ray spectrum is known to fall off more rapidly than the pion spectrum, the electron contamination will decrease with increasing energy. The effect of these contaminations on the measured cross sections was negligible. The muon contamination was measured at each momentum, although, as will be shown later in this section, the experimental method obviated the need for any correction.

A pressure-controlled double-jacketed 2-ft-long liquid-hydrogen target was used. The target-cell windows were made of 0.006-in. Mylar and the surrounding vacuum box had 0.010-in. Mylar windows. In addition, there were 40 layers of 0.00025-in. aluminized Mylar as a radiation shield. The length of the full hydrogen target was measured optically with an accuracy of ± 0.02 in. The pressure was controlled to be within the range 17.8–18.0 psi, corresponding to a density of $0.6997 \text{ g/cm}^3 \pm 0.03\%$.

The general features of the construction of the hodoscopes were similar to those described earlier.⁸ RCA 7767 photomultiplier tubes were used for the $\frac{1}{8}$ -in.-wide scintillators and RCA 6199 photomultiplier tubes were used for the larger sizes. Lucite light pipes were used in all cases.

Since this experiment measured scattering in and near the region dominated by Coulomb scattering, the usual technique of applying a correction for muon contamination on the basis of a separate measurement of the contamination would have involved an angular dependent subtraction as well as an over-all scale shift. Consequently, it was decided to use a muon-rejection system placed at the end of the apparatus to reject all muons at that point. It consisted of 6 ft of steel plus 2 ft of lead followed by four scintillation counters, each 24×18 in., placed side by side perpendicular to the beam. This was placed behind H4 in such a position as to maximize the efficiency of muon detection over this screen. The efficiency was measured by a procedure to be described in Sec. III, using a broad

muon beam produced by raising 8 ft of steel into the beam just behind the hydrogen target. The efficiency of muon rejection was $\sim 99\%$ at the beam height and $>95\%$ in all other regions. The fraction of muons in the beam varied from 6.5% at 8 GeV/c to 2.7% at 26 GeV/c. The small inefficiency in the rejection system produced an error of $<0.1\%$ in the final cross sections.

The magnet power supplies were rated at 0.1% regulation and the magnet currents were monitored throughout the experiment. In addition, the bending magnets contained calibrated Hall probes. During the runs, a system of relays cycled automatically through the various magnet currents, Hall currents and Hall voltages, one reading being taken each AGS pulse with a digital voltmeter and transmitted with the on-line data to the PDP-6 computer. The computer and its peripheral equipment were located in a pair of trailers near the apparatus. Because of its large memory (65,536 words, each 36 bits) and the time-sharing system, the computer was capable of monitoring the magnets and doing on-line analysis of the events while simultaneously running subsidiary programs.

The trigger system was designed to permit the whole region of interest to be studied with the same electronic and physical arrangement (see Fig. 2). A coincidence between the counters defining the incident beam, the region of H2 outside the beam and H4, provided the signal-to-gate 144 “discriminator-coincidence-buffer” circuits (fast gates) in order to interrogate all the counters and so determine which had been struck. The resolving time of the fast gates was 20 nsec. The contents of the fast gates were then transferred within 15 μ sec to a buffer memory with a 2030-event capacity. At the end of each AGS pulse, the contents of the memory were transferred to the PDP-6 computer for on-line analysis and in parallel on to magnetic tape for a permanent record. Because of the 15- μ sec dead time of the data-handling system, not all triggers could be accepted. Since the triggers were scaled independently of the data-handling system, the fraction accepted was known and the absolute normalization of the data could be obtained.

A block diagram of the main system of electronics is shown in Fig. 2. In most cases the circuits used were from the Chronetics Nanologic 100 system, but in the anticoincidence channels dc coupled EG and GM100 series units were used. The resolution (2τ) of the beam identification channel was 5 nsec while the trigger logic had a resolving time of 20 nsec. Various monitor channels are not shown. All scaler information was transmitted with the data on to magnetic tape and to the computer at the end of each AGS pulse. The system of electronics shown in Fig. 3 was used to reduce accidental effects. Signals from each counter in one plane of an incident hodoscope were shaped and added linearly. A discriminator set 2 dB above the single pulse level fired whenever more than one particle struck

⁶ S. J. Lindenbaum, W. A. Love, S. Ozaki, J. J. Russell, and L. C. L. Yuan, Nucl. Instr. Methods **20**, 256 (1963).

⁷ H. M. Roder, D. E. Diller, L. A. Weber, and D. R. Goodwin, Cryogenics **3**, 16 (1963).

⁸ K. J. Foley, S. J. Lindenbaum, W. A. Love, S. Ozaki, J. J. Russell, and L. C. L. Yuan, Nucl. Instr. Methods **30**, 45 (1964).

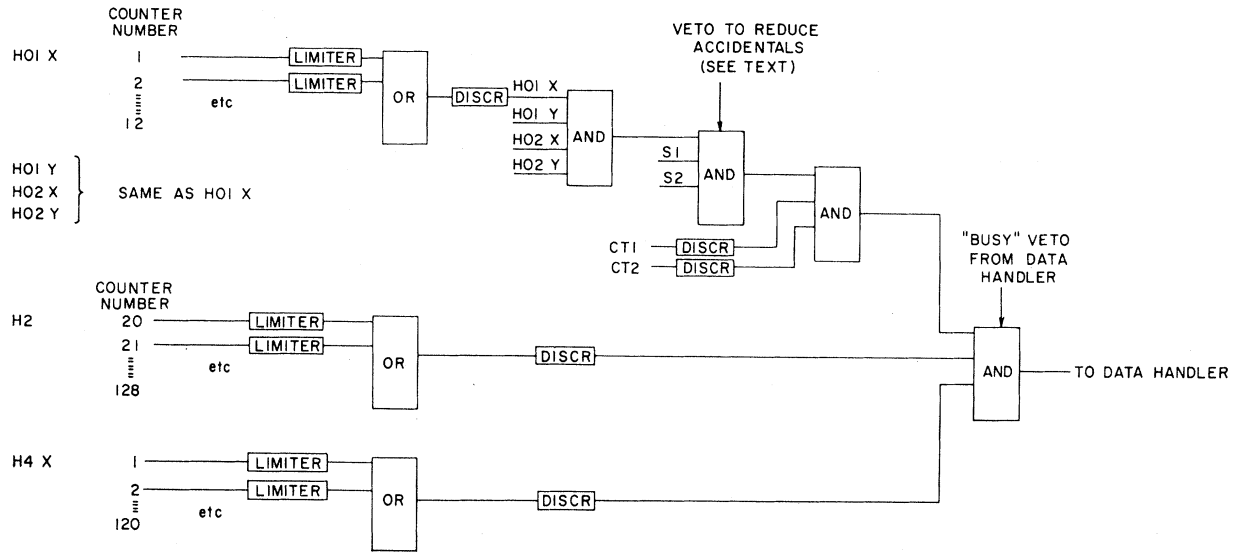


Fig. 2. Main system of electronics.

the plane within the trigger-logic resolving time. These veto signals from all four incident planes, plus signals from the ring veto counters shown in Fig. 1, were fed to an OR circuit giving one signal to reject events where more than one incident particle arrived within the fast-gate resolving time. In order to monitor the remaining accidental effects, summed signals from each hodoscope screen were delayed by one radio-frequency period of the AGS and fed into separate fast gates.

The fast gates were operated at 20-nsec full width in order to reduce the severity of the timing requirements on the several hundred scintillation-counter hodoscope elements used in this experiment. The rough timing of the scintillation counters was accomplished by observing pulses with a Tektronix 585A oscilloscope,

and the final timing of each counter was set to ± 0.5 nsec using the special delay curves described in Sec. III.

In order to reduce the number of gates needed to handle the scintillation counters, coding systems were used for all but the smallest hodoscopes. For example, H4X was divided up into 12 successive regions, each containing 10 counters. The signal from each counter was split electronically to follow two paths. OR circuits were then used to generate two sets of signals. One signal for the sum of each of the groups of 10 counters (giving 12 signals) and another from the sum of all counters at a particular location within a group (a further 10 signals). Thus, one signal indicated the group containing the counter struck and the other signal gave the location within the group. Therefore,

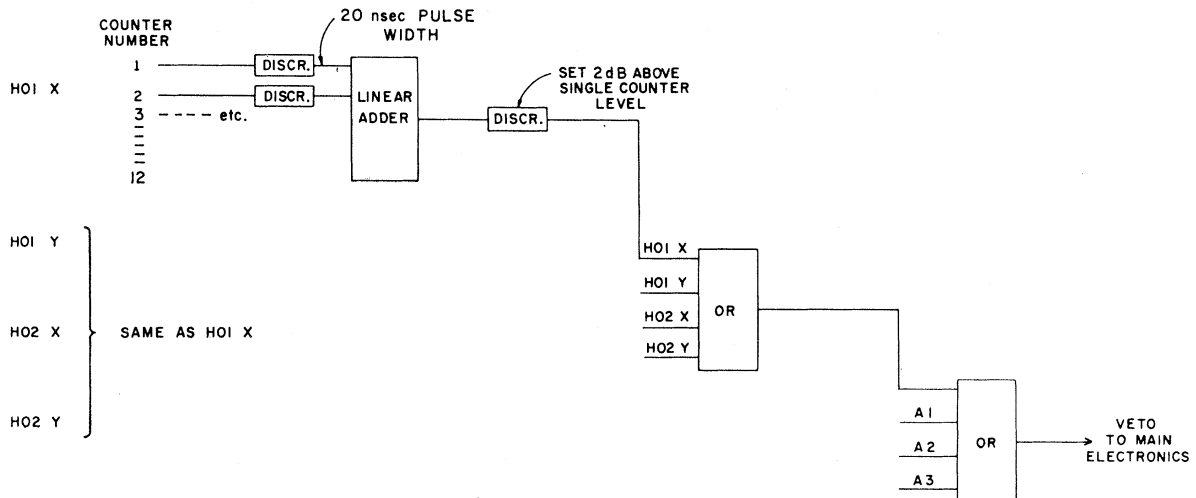


Fig. 3. System used to reduce accidental coincidences.

22 gates were needed to define 120 counters. Of course, there was an ambiguity when several particles hit any screen, but for the purpose of this experiment (elastic and near-elastic scattering) such events were of no interest and were rejected.

The counters were moved for the final 30% of the run to cover a wider angular region (0–27 mrad, as opposed to the 0–22 mrad for the first setup) with mean over-all angular and momentum resolutions of 0.5 mrad and 0.4%. These runs were analyzed separately and used as a check on the experiment by measuring at momenta, overlapping those studied in the earlier arrangement. The results agreed within statistics, indicating that the corrections for the effects of finite angular resolution were accurate.

III. EXPERIMENTAL PROCEDURE

A. Data Taking

For the on-line computer operations, a single large program was written that incorporated all the monitoring functions of the computer, including full analysis of the events, to produce an elastic differential cross section for each scattering angle bin. This program accepted input either on-line from a data link between the computer and the data handler or off-line from magnetic tape. Each event consisted of 144 binary bits of information. The program unpacked the data and, if the hodoscopes showed the passage of only one particle, it reconstructed the angle of scatter, the momentum of the particle, and the point of interaction along the beam. Complete analysis of one event took 4 msec and, since the data acquisition rate was as high as 2000 events each 2.5 sec, on-line analysis of all events was not possible. Hence, only a fraction of the data was analyzed on-line and the complete off-line analysis from tape was kept as current as possible. The computer was operated continuously and this, together with the logistics of the AGS scheduling, enabled us to analyze all the data with less than two weeks delay.

After each beam spill, 16 words were added to the hodoscope information that had been stored in the data handler. These "special" words included the scaler readings, a digital clock, and the reading of a digital voltmeter (DVM) which stepped, one step per AGS burst, through a number of voltage-monitoring tasks. The voltages monitored included a standard cell to check the DVM, all the quadrupole and dipole magnet shunt voltages, the current and voltage readings of Hall probes in all the dipole magnets, and the readings of pressure transducers in the Cherenkov counters. For its on-line monitoring functions, the computer analyzed all the special words in each pulse; in every eighth or sixteenth pulse, it analyzed all of the events in an entire buffer memory dump. A teletype message was printed when any of the voltages varied outside of tolerance or when the centering of the beam drifted, as signaled by

the scaler rates for three beam-locating counters in the hodoscope H4 onto which the beam was directed. The magnet tolerances were usually 0.1% and the Cherenkov-counter pressure tolerance was 2%. This function was crucial since good magnet stability was essential to the operation of this high-resolution experiment.

As each run was terminated, a computer printout of the on-line analysis was obtained. The information provided was as follows:

- (a) Identifying labels, run number, target full or empty, momentum and charge of beam particles, and date and time of data taking, etc.
- (b) Total number of events analyzed, broken down according to whether any hodoscopes were missed or had multiple triggers, and the number removed by various fiducial cuts.
- (c) All parameters and constants used in the analysis.
- (d) Properties of the beam, such as the mean angle of incidence and the momentum spread.
- (e) Final readings of all scalers and various counting rate ratios of interest.
- (f) The nominal settings of each monitored voltage, the maximum excursion during the run, the mean and rms spread, and the number of readings of each voltage.
- (g) A tabulation of accidental coincidence rates provided by analyzing the delayed signals described in Sec. II.
- (h) The number and fraction of events that were registered as single, missing, or multiple in each hodoscope screen, considered separately and in certain physically meaningful combinations.
- (i) A histogram of the number of counts in each counter and in each fast gate.
- (j) The momentum spectrum for each of 30 angular bins.
- (k) A table of cross sections and errors versus angle.

B. Special Types of Runs

In addition to the data runs, various special runs were analyzed by special programs or by modification of the analysis program. These included the following:

- (i) Accidental runs. In these the gate trigger was delayed by one AGS rf period. A subroutine which could be called by the regular program calculated the accidental rates.
- (ii) Muon veto counter-efficiency runs. In these runs, 8 ft of steel was raised into the beam just downstream of the hydrogen target and the broad muon beam thus produced was spread by the bending magnets over the back screen. The probability that any count occurring in H4 was accompanied by a count in a muon counter was determined for 30 different areas of H4: This is a direct measure of the muon rejection efficiency.
- (iii) Delay curves of the hodoscope counters. A special program was used that saved the total number

of counts in each of the 408 counters for a number of different delays of the fast-gate trigger. At the conclusion of the series of runs, the delay curve for any individual counter could be displayed on the cathode ray tube attached to the computer; using a light pen one could page rapidly through the delay curves for the hole hodoscope array. This system enabled us to set the timing of each counter to ± 0.5 nsec.

(iv) Beam profile runs. For this type of run the beam was bent onto H4 with H2 and H4 removed from the trigger and with the hydrogen target empty, so that the properties of the incident beam could be studied. For each new momentum the beam momentum spread and the angle between the mean beam direction and the axis of the apparatus was minimized and the flux was maximized by adjustment of the quadrupole and bending magnets, using the computer on-line to measure the momentum and angular spread of the beam. These profile runs were repeated periodically to monitor the incident beam conditions. For these runs the analysis program was used practically unchanged.

(v) Hodoscope efficiency runs. These runs were a reanalysis of the beam profile runs, programatically rejecting all incident particles except those in the central core of the beam. The number of events within the elastic-peak region of the momentum spectrum was then a measure of the over-all detection efficiency of the hodoscope system, including rejection of pions that decayed before H4. This measurement was made several times during each set of runs at each momentum. After correction for accidentals, muon contamination, and pion decay, the efficiency was very nearly constant over the experiment. In addition, on various occasions during the experiment, the hodoscopes H2 and H4 were moved in turn across the beam 1 in. at a time and the efficiency was measured at each position. Variations in efficiency caused fluctuations much smaller than the statistical errors on the final differential cross sections. By rotating H2, we established that its efficiency changed by less than 0.1% when the angle of incidence of the particle was changed by 30 mrad. Continuous monitoring of the counters was achieved by observing the histograms of the number of counts in each counter during the actual data runs. Experience showed that any poor counter performance which would not be observable in the counter profiles would produce an error in the final cross sections much smaller than the statistical errors on the cross sections. Of course, a small uniform over-all shift of counter efficiency would not have shown up in the counter profiles, but such a possibility was ruled out by the frequent efficiency runs.

IV. CALCULATION OF THE DIFFERENTIAL CROSS SECTIONS

A. Data Analysis

The final data were obtained by analysis of the magnetic tape records. The analysis of an individual

event will now be described in some detail. The number of counters struck in each hodoscope screen was recorded as part of the monitoring function, but no attempt was made to reconstruct an event unless there was one and only one counter signal in each screen except H1, the "target-test" hodoscope. If the "single trigger" test was satisfied in all four hodoscope screens in front of the liquid-hydrogen target, then the event was added to the sum of "good incident" events used later for calculating absolute cross sections.

The scattering angle was calculated assuming that the particle scattered once in the center of the liquid-hydrogen target and passed through the center lines of the triggered counters in H2 (x coordinate) and H4 (y coordinate). The alignment of H1X, H1Y, H2, and H4Y counters was checked with each profile run by measuring the centroids of the distributions of counts in each screen for particles which passed through H01 and H02 parallel to the axis of the beam.

The momentum of the scattered particle was calculated from the center of the H4X counter struck. The momentum calibration was maintained by keeping the unscattered beam always centered on the same H4X counter.

If either H1X or H1Y or both had a single counter triggered, the target test was applied. The projected area in which the scattering could have taken place was computed and if it did not overlap the hydrogen target, the event failed the target test. The program also checked whether the particle events had hit a muon counter. The data were recorded in separate sets of angular bins depending on whether the counter struck in H2 was 0.127 or 0.266 in. wide. In the first set up, for the 0.127-in. counters the bins were 0.5 mrad wide, ranging from 0 to 6 mrad; for the 0.266-in. counters, the bins were 1.0 mrad wide and covered the range 4–22 mrad. In the second set up, the 0.127-in. counters had bins 0.6 mrad wide from 0 to 9 mrad and the 0.266-in. counters had bins 1.4 mrad wide from 7 to 28 mrad. For each angular region a 56-bin momentum spectrum was constructed. The momentum bin width selected varied from 0.25% at 8 GeV/ c to 0.15% at 26 GeV/ c . Three separate spectra of events versus angle and momentum were stored. The first had no target test applied and the second had those events which failed the target test removed. For these two spectra, events where a particle had hit a muon counter were removed. The third spectrum was the same as the second except that "muon" events were not removed. After a run had been analyzed, the spectra were recorded on DECTape, together with identifying information, scalar totals, etc. Sets of runs at each momentum were collected together from the data on the DECTape by a separate summing program which formed spectra $d^2\sigma/dpd\Omega$ for target full runs, target empty runs, and net "hydrogen" effect. The counts in the elastic peak were then summed to give elastic differential cross sections.

The solid angle represented by each angular bin was computed by a separate program which calculated, for the measured geometry, the number of combinations of H2 and HY4 counters which were put into each angular bin for each incident channel, i.e., each combination of H01X, H01Y, H02X, H02Y counters. This result was then folded with the actual incident beam distribution, as measured by the profile runs, to produce the solid angles for each angular bin for each momentum and set up. A 2.5% correction was applied to allow for dipole focussing in the analyzing magnets.

The effective value of the negative square of the four-momentum transfer t was calculated for each angular bin by a Monte Carlo program which took into account the geometry of the apparatus and the angular distribution. This program also calculated solid angles for the bins. These agreed with the more accurate direct calculations described above within the Monte Carlo statistical errors.

The t values and solid angles for the set of runs being analyzed were read into the summing program from paper tape and the program then calculated absolute differential cross sections by means of the formula

$$\frac{d\sigma}{d\Omega} = \frac{N_{e1}}{\epsilon T d\Omega N_{inc} R_1 R_2}, \quad (1)$$

where N_{e1} is the number of events in the elastic peak, N_{inc} is the number of incident particles recorded on the scalars, T is the target thickness, $d\Omega$ the solid angle of the bin, and ϵ is the measured net particle detection efficiency. R_1 is the ratio of the number of events analyzed to the trigger scaler reading, and R_2 is the fraction of analyzed events which were "good" in all the incident hodoscope screens. Thus R_1 corrects for deadtime in the data handler while R_2 corrects for inefficiencies in the incident screens. Straightforward relativistic kinematics are then used to derive $d\sigma/dt$.

B. Corrections

Accidentals were measured regularly in special runs with the trigger delayed one rf period and monitored continuously with delayed bits introduced in each event. The net correction for accidentals was 0.2%-1% for the π^+ measurements and negligible for the π^- runs. We estimate that the systematic error is smaller than 20% of the accidental corrections.

The efficiencies used in the final cross-section calculations were taken from a smooth curve drawn through a plot of the measured efficiencies versus incident momentum. The uncertainty in the efficiency, as estimated from the deviations from the smooth curve of the actual measurements over the whole period of the experiment, amounts to $\pm 1\%$ on the absolute cross sections, of which we estimate one-half to be momentum-independent. The target-full runs were corrected at each momentum for multiple interactions of the pions

on the basis of the pion-proton total cross sections. The size of the correction was approximately 7%.

We applied a small correction for nonelastic events under the elastic peaks in the momentum spectra on the basis of an extrapolation of the background to the pion-production threshold. The size of the correction was $\lesssim 1\%$. We estimate the uncertainty in this correction to be less than 0.2%. As described above, the procedure for determining the value of t unfolded the effects of the angular and momentum resolution. In order to present values of the differential cross sections in a form suitable for comparison with theory, we have also corrected the raw data for multiple-scattering effects. Multiple- and plural-scattering corrections were calculated by using a Molière distribution⁹ modified to apply to the pion-hydrogen case. In the notation of Ref. 9, we have included $f^{(0)}$ (the Gaussian term), $f^{(1)}$, and $f^{(2)}$. In the region of interest, $f^{(3)}$ was found to be negligible. The Molière distribution was modified to take account of the fact that the experimental momentum resolution eliminated events in which pions scatter from electrons with $|t| > 10^{-4}$ (GeV/c)². It was also necessary to modify the distribution to take account of the target test which eliminated the nonhydrogen single scatters. This modification was necessary because at small angles there is not complete cancellation of the nonhydrogen events in an empty target subtraction, since, when the target is full the distribution from the nonhydrogen background is broadened by the presence of the hydrogen. The target-test correction was of the order of 7% of $f^{(1)}$ at 10 GeV/c and at $|t| = 0.001$ (GeV/c)², and fell off with increasing energy and with increasing $|t|$. The complete multiple-scattering correction was as large as 30% of the pure Coulomb scattering at $|t| = 0.001$ (GeV/c)² and fell off rapidly with increasing $|t|$ to about 5% at $|t| = 0.005$ (GeV/c)². One should note that previously published multiple-scattering calculations¹⁰ do not apply directly to the pion-hydrogen case at high energies. It was refinements in these and other electromagnetic effects that were the major causes of slight differences between early results^{5,11} and the present final results.

V. DIFFERENTIAL CROSS SECTIONS

The measured cross sections and their errors are given for each momentum in Table II along with the t values and the cross sections after multiple-scattering, vacuum-polarization, and radiative corrections¹² have been applied. Typical corrected cross sections are also shown in Figs. 4 and 5. The momenta in Table II

⁹ G. Molière, *Z. Naturforsch* **3A**, 78 (1948); H. A. Bethe, *Phys. Rev.* **89**, 1256 (1953).

¹⁰ U. Fano, *Phys. Rev.* **93**, 117 (1954).

¹¹ S. J. Lindenbaum, in *Proceedings of the Irvine Conference on π -N Scattering*, 1967 (unpublished).

¹² G. B. West and D. R. Yennie, *Phys. Rev.* **172**, 1413 (1968). We wish to thank the authors for private communications and valuable discussions.

TABLE II. Measured differential cross sections. The momenta marked with an asterisk (*) indicate measurements made with the second arrangement of the apparatus which included larger scattering angles than the first. The measurements with the first arrangement with $|t|$ values less than 0.001 have been cut off in order to keep the multiple scattering corrections small. For the second arrangement the cutoff was chosen as 0.002. The uncorrected measurements are given only to show the net magnitude and t dependence of the corrections described in the text. Since the corrections are subtractions from the measurements, the error indicated applies to either column of cross sections. At each momentum a systematic scale uncertainty of $\pm 0.5\%$ must be applied together with an additional 0.5% momentum-independent scale uncertainty.

$-t$ [(GeV/c) ²]	$d\sigma/dt$ (uncorrected) [mb/(GeV/c) ²]	Error [mb/(GeV/c) ²]	$d\sigma/dt$ [mb/(GeV/c) ²]	$-t$ [(GeV/c) ²]	$d\sigma/dt$ (uncorrected) [mb/(GeV/c) ²]	Error [mb/(GeV/c) ²]	$d\sigma/dt$ [mb/(GeV/c) ²]
7.89* GeV/c π^-				9.89* GeV/c π^-			
0.00231	81.74	4.09	75.31	0.04588	23.47	0.79	23.12
0.00278	62.85	3.53	59.21	0.05207	24.03	0.79	23.64
0.00330	54.97	3.30	52.81	0.05856	21.89	0.75	21.51
0.00387	46.79	3.37	45.42	0.06546	20.67	0.71	20.27
0.00448	42.90	3.52	41.99	11.89 GeV/c π^-			
0.00515	45.32	4.26	44.67	0.00110	293.3	11.2	230.9
0.00381	49.55	3.79	48.12	0.00145	167.50	6.46	142.18
0.00519	41.26	2.30	40.63	0.00181	113.80	4.45	101.50
0.00687	39.00	1.86	38.64	0.00225	77.38	3.27	71.19
0.00880	36.57	1.73	36.31	0.00270	64.96	2.83	61.44
0.01100	36.27	1.60	36.04	0.00323	51.66	2.44	49.60
0.01347	34.14	1.52	33.91	0.00380	47.65	2.47	46.36
0.01616	33.54	1.46	33.30	0.00441	38.74	2.42	37.89
0.01908	32.57	1.39	32.32	0.00509	39.03	2.51	38.43
0.02225	31.31	1.32	31.04	0.00577	41.17	2.89	40.71
0.02567	29.81	1.23	29.53	0.00435	42.15	2.38	41.26
0.02935	26.86	1.14	26.58	0.00598	37.47	1.56	37.05
0.03325	27.58	1.15	27.26	0.00792	31.95	1.25	31.69
0.03744	28.75	1.13	28.38	0.01019	31.29	1.16	31.08
0.04181	24.84	1.07	24.49	0.01278	31.39	1.09	31.19
9.84 GeV/c π^-				0.01559	29.91	1.04	29.70
0.00124	230.34	8.45	188.88	0.01871	28.58	0.98	28.35
0.00154	147.91	5.80	127.84	0.02213	28.14	0.94	27.90
0.00186	110.90	4.71	99.84	0.02588	28.06	0.91	27.79
0.00222	79.58	3.80	73.23	0.02977	25.85	0.85	25.57
0.00260	68.00	3.58	64.10	0.03397	25.11	0.83	24.81
0.00302	54.68	3.49	52.21	0.03852	25.25	0.80	24.92
0.00347	54.38	3.57	52.73	0.04335	22.54	0.75	22.22
0.00398	51.31	4.17	50.19	0.04845	22.65	0.73	22.31
0.00299	60.25	3.55	57.69	14.16 GeV/c π^-			
0.00409	41.81	2.10	40.77	0.00114	261.1	14.0	204.9
0.00543	37.63	1.67	37.13	0.00156	152.63	7.92	132.55
0.00695	35.98	1.53	35.66	0.00204	86.39	5.10	77.80
0.00870	33.61	1.46	33.38	0.00258	66.36	3.93	62.25
0.01061	30.87	1.36	30.67	0.00319	54.70	3.43	52.53
0.01272	30.25	1.30	30.06	0.00386	46.91	3.05	45.66
0.01511	31.72	1.28	31.50	0.00462	40.92	2.93	40.15
0.01770	30.75	1.26	30.53	0.00538	36.35	3.02	35.83
0.02033	29.91	1.20	29.67	0.00627	35.83	3.07	35.45
0.02330	31.15	1.20	30.88	0.00722	34.74	3.30	34.45
0.02637	28.21	1.11	27.93	0.00817	31.61	3.70	31.36
0.02973	26.70	1.08	26.42	0.00621	36.06	2.90	35.67
0.03324	28.02	1.08	27.70	0.00853	30.72	1.83	30.49
9.89* GeV/c π^-				0.01124	31.45	1.54	31.25
0.00234	76.94	3.33	70.42	0.01448	27.60	1.36	27.41
0.00294	59.64	2.68	56.44	0.01811	29.68	1.34	29.46
0.00360	48.01	2.34	46.27	0.02213	28.05	1.27	27.81
0.00436	43.19	2.18	42.17	0.02652	27.30	1.22	27.03
0.00518	37.74	2.11	37.10	0.03131	25.31	1.15	25.03
0.00607	33.98	2.12	33.54	0.03651	23.88	1.07	23.59
0.00703	33.47	2.38	33.14	0.04224	22.13	1.00	21.82
0.00803	34.33	2.63	34.05	0.04825	22.92	1.02	22.57
0.00595	37.34	2.47	36.87	0.05455	19.82	0.92	19.49
0.00814	34.44	1.58	34.17	0.06133	20.21	0.93	19.84
0.01080	32.90	1.25	32.68	0.06859	18.83	0.87	18.46
0.01382	31.82	1.14	31.60	15.99 GeV/c π^-			
0.01728	30.74	1.08	30.51	0.00101	358.6	17.9	272.8
0.02109	29.03	1.00	28.79	0.00145	161.38	7.35	135.41
0.02533	27.25	0.94	26.99	0.00198	94.78	4.00	85.24
0.02989	26.86	0.91	26.57	0.00260	65.69	2.70	61.64
0.03483	27.43	0.89	27.10				
0.04025	23.97	0.82	23.65				

TABLE II (continued)

$-t$ [(GeV/c) ²]	$d\sigma/dt$ (uncorrected) [mb/(GeV/c) ²]	Error [mb/(GeV/c) ²]	$d\sigma/dt$ [mb/(GeV/c) ²]	$-t$ [(GeV/c) ²]	$d\sigma/dt$ (uncorrected) [mb/(GeV/c) ²]	Error [mb/(GeV/c) ²]	$d\sigma/dt$ [mb/(GeV/c) ²]
15.99 GeV/c π^-				18.19* GeV/c π^-			
0.00328	50.99	2.10	48.96	0.10126	13.25	0.30	12.91
0.00408	43.72	1.77	42.63	0.11828	11.36	0.27	11.04
0.00492	37.61	1.59	36.96	0.13641	10.19	0.25	9.89
0.00585	33.71	1.51	33.28	0.15600	8.35	0.22	8.08
0.00691	32.62	1.53	32.30	0.17636	7.52	0.20	7.26
0.00797	33.35	1.56	33.09	0.19848	6.24	0.18	6.01
0.00920	31.37	1.62	31.15	0.22170	5.24	0.16	5.03
0.01043	29.42	1.93	29.23				
0.00789	32.53	1.52	32.27				
0.01086	28.89	1.00	28.70				
0.01442	28.05	0.83	27.86				
0.01857	27.29	0.75	27.07				
0.02307	26.28	0.70	26.04				
0.02824	24.44	0.64	24.19				
0.03378	23.42	0.60	23.14				
0.04009	22.54	0.57	22.24				
0.04671	21.14	0.55	20.82				
0.05384	20.30	0.52	19.96				
0.06140	18.57	0.49	18.23				
0.06953	17.20	0.46	16.85				
0.07840	16.00	0.43	15.65				
0.08767	15.22	0.43	14.87				
16.00* GeV/c π^-				20.15 GeV/c π^-			
0.00248	71.91	3.22	65.81	0.00100	364.1	25.8	275.1
0.00350	48.34	1.92	46.27	0.00159	140.44	8.37	120.85
0.00476	38.41	1.44	37.55	0.00230	80.64	4.28	74.51
0.00613	33.89	1.21	33.43	0.00313	54.25	2.79	51.86
0.00773	30.50	1.08	30.21	0.00414	42.85	2.16	41.79
0.00952	30.84	1.03	30.61	0.00523	36.70	1.87	36.13
0.01148	29.00	0.97	28.80	0.00648	32.78	1.70	32.42
0.01364	26.52	0.93	26.34	0.00783	30.45	1.54	30.19
0.01592	28.05	0.97	27.84	0.00938	28.04	1.50	27.83
0.01837	26.98	1.02	26.77	0.01093	28.93	1.57	28.73
0.02104	26.81	1.13	26.58	0.01273	27.97	1.58	27.78
0.01581	26.85	1.03	26.65	0.01459	29.29	1.70	29.09
0.02150	26.31	0.69	26.08	0.01650	27.03	1.93	26.83
0.02825	24.76	0.56	24.51	0.01259	29.24	1.47	29.05
0.03620	23.08	0.50	22.79	0.01733	26.52	0.98	26.32
0.04518	21.33	0.46	21.02	0.02293	25.39	0.81	25.16
0.05521	19.32	0.42	18.99	0.02938	23.79	0.72	23.54
0.06626	17.23	0.38	16.89	0.03672	22.25	0.67	21.97
0.07805	15.80	0.36	15.46	0.04481	20.79	0.62	20.49
0.09106	14.49	0.33	14.15	0.05359	19.12	0.58	18.81
0.10527	12.80	0.31	12.47	0.06334	17.42	0.54	17.10
0.12028	11.00	0.28	10.69	0.07394	15.95	0.50	15.62
0.13636	9.91	0.26	9.61	0.08543	14.69	0.47	14.35
0.15304	8.86	0.24	8.57	0.09770	13.00	0.44	12.68
0.17122	7.21	0.21	6.96	0.11071	11.53	0.40	11.22
				0.12419	10.20	0.38	9.91
				0.13889	9.68	0.36	9.39
18.19* GeV/c π^-				20.38 GeV/c π^-			
0.00209	99.75	5.58	88.92	0.00104	336.5	21.3	257.9
0.00319	54.36	2.53	51.52	0.00163	131.33	6.52	113.18
0.00455	39.95	1.63	38.95	0.00237	72.76	3.05	67.18
0.00613	33.58	1.27	33.12	0.00324	52.25	1.94	50.10
0.00796	31.05	1.10	30.77	0.00423	40.63	1.40	39.63
0.01006	30.66	1.01	30.44	0.00537	36.31	1.17	35.77
0.01229	28.50	0.92	28.30	0.00662	33.02	1.02	32.67
0.01485	28.33	0.89	28.13	0.00801	30.67	0.95	30.42
0.01768	28.43	0.89	28.21	0.00957	29.65	0.90	29.44
0.02054	26.68	0.87	26.46	0.01119	27.45	0.85	27.26
0.02391	26.07	0.91	25.83	0.01303	27.98	0.88	27.79
0.02740	26.10	0.99	25.84	0.01490	28.67	0.91	28.47
0.02057	26.00	0.94	25.78	0.01697	28.14	1.01	27.93
0.02777	25.00	0.63	24.74	0.01304	26.93	0.85	26.75
0.03667	23.12	0.50	22.83	0.01786	26.22	0.60	26.02
0.04693	21.33	0.44	21.01	0.02345	24.76	0.50	24.54
0.05868	19.14	0.40	18.80	0.02998	23.58	0.45	23.32
0.07162	17.20	0.37	16.86	0.03738	21.91	0.41	21.63
0.08581	15.09	0.33	14.74	0.04586	20.00	0.37	19.70
				0.05507	18.66	0.34	18.34
				0.06499	17.53	0.32	17.19
				0.07564	15.63	0.30	15.30
				0.08717	13.85	0.27	13.53
				0.09977	12.49	0.25	12.17
				0.11332	11.23	0.23	10.93
				0.12728	10.04	0.21	9.75
				0.14199	8.74	0.19	8.47
18.19* GeV/c π^-				22.13 GeV/c π^-			
				0.00122	245.7	17.9	199.3
				0.00191	98.76	6.17	87.77

TABLE II (continued)

$-t$ [(GeV/c) ²]	$d\sigma/dt$ (uncorrected) [mb/(GeV/c) ²]	Error [mb/(GeV/c) ²]	$d\sigma/dt$ [mb/(GeV/c) ²]	$-t$ [(GeV/c) ²]	$d\sigma/dt$ (uncorrected) [mb/(GeV/c) ²]	Error [mb/(GeV/c) ²]	$d\sigma/dt$ [mb/(GeV/c) ²]
22.13 GeV/c π^-				26.23 GeV/c π^-			
0.00279	59.48	3.29	56.09	0.06222	16.69	0.39	16.38
0.00381	45.65	2.22	44.29	0.07578	15.03	0.36	14.71
0.00504	36.47	1.78	35.84	0.09073	13.02	0.32	12.71
0.00635	33.75	1.55	33.38	0.10743	11.26	0.29	10.96
0.00778	30.39	1.43	30.13	0.12549	10.05	0.27	9.76
0.00946	28.11	1.33	27.90	0.14477	8.37	0.24	8.11
0.01126	27.78	1.28	27.59	0.16533	6.97	0.21	6.73
0.01322	27.68	1.29	27.50	0.18698	5.82	0.19	5.61
0.01533	27.65	1.31	27.45	0.21044	5.15	0.17	4.95
0.01751	29.11	1.49	28.89	0.23535	4.17	0.15	4.01
0.01991	27.16	1.59	26.94				
0.01536	28.06	1.23	27.86	7.76* GeV/c π^+			
0.02096	25.42	0.84	25.21	0.00222	103.12	5.64	95.85
0.02765	23.88	0.68	23.64	0.00269	84.50	4.97	80.49
0.03550	21.88	0.59	21.61	0.00319	74.95	4.79	72.54
0.04445	20.57	0.55	20.27	0.00374	65.18	4.65	63.65
0.05410	18.53	0.50	18.23	0.00434	61.08	5.10	60.05
0.06467	16.46	0.46	16.09	0.00497	44.63	5.92	43.93
0.07648	15.99	0.45	15.65	0.00366	67.34	5.06	65.71
0.08927	14.01	0.41	13.68	0.00503	49.96	3.04	49.26
0.10290	12.28	0.37	11.97	0.00662	43.05	2.32	42.66
0.11744	11.04	0.35	10.73	0.00851	41.67	2.11	41.39
0.13310	9.51	0.31	9.22	0.01063	35.86	1.95	35.63
0.14970	8.21	0.29	7.95	0.01299	35.38	1.83	35.15
0.16767	7.02	0.26	6.79	0.01559	34.00	1.71	33.76
				0.01844	33.21	1.66	32.95
24.22 GeV/c π^-				0.02151	32.35	1.58	32.08
0.00146	165.6	12.1	139.0	0.02484	30.36	1.54	30.07
0.00231	75.95	4.62	69.79	0.02836	27.78	1.43	27.49
0.00332	48.14	2.64	46.11	0.03216	28.60	1.40	28.28
0.00453	39.31	1.92	38.47	0.03621	26.45	1.31	26.13
0.00596	32.87	1.56	32.44	0.04042	26.76	1.32	26.40
0.00756	30.95	1.37	30.68				
0.00939	28.99	1.29	28.78	9.86 GeV/c π^+			
0.01134	28.83	1.19	28.64	0.00125	265.4	12.0	225.7
0.01357	26.29	1.14	26.11	0.00155	187.25	8.83	167.48
0.01582	27.93	1.18	27.73	0.00187	143.06	7.38	132.17
0.01839	25.61	1.16	25.41	0.00224	108.06	6.20	101.89
0.02111	25.95	1.32	25.74	0.00264	85.04	5.68	81.29
0.02393	24.04	1.44	23.82	0.00303	79.46	5.65	76.99
0.01829	25.15	1.07	24.95	0.00349	62.69	5.68	61.04
0.02508	24.92	0.76	24.68	0.00396	61.49	6.78	60.33
0.03309	21.95	0.60	21.69	0.00296	81.40	5.50	78.75
0.04252	20.91	0.54	20.62	0.00413	59.79	3.33	58.75
0.05313	18.44	0.49	18.14	0.00546	44.83	2.53	44.31
0.06478	16.86	0.45	16.54	0.00700	37.50	2.24	37.18
0.07755	14.98	0.41	14.66	0.00874	36.02	2.07	35.77
0.09159	13.31	0.38	13.00	0.01067	35.10	2.00	34.88
0.10692	11.66	0.34	11.36	0.01283	29.93	1.81	29.73
0.12364	10.02	0.31	9.73	0.01517	32.10	1.84	31.88
0.14119	8.65	0.29	8.38	0.01777	34.52	1.79	34.26
0.15990	7.79	0.27	7.53	0.02041	28.87	1.65	28.63
0.17972	6.77	0.25	6.53	0.02333	29.54	1.57	29.27
0.20099	5.38	0.21	5.18	0.02644	29.45	1.48	29.16
				0.02985	29.48	1.47	29.17
				0.03333	25.91	1.36	25.61
26.23 GeV/c π^-							
0.00172	123.46	8.86	107.84	10.02* GeV/c π^+			
0.00269	61.76	3.56	57.88	0.00241	98.83	2.92	92.83
0.00392	42.77	2.11	41.50	0.00304	75.26	2.26	72.33
0.00532	33.48	1.52	32.92	0.00372	61.95	1.89	60.34
0.00701	30.72	1.28	30.41	0.00450	54.46	1.71	53.51
0.00889	28.52	1.12	28.30	0.00532	44.68	1.57	44.06
0.01103	28.15	1.03	27.96	0.00623	44.99	1.60	44.54
0.01332	26.15	0.95	25.97	0.00723	37.89	1.65	37.56
0.01589	26.15	0.92	25.96	0.00828	39.28	1.88	39.00
0.01856	25.19	0.93	24.99	0.00612	40.78	1.64	40.33
0.02158	24.55	0.91	24.34	0.00841	37.11	1.07	36.84
0.02474	23.93	0.99	23.70	0.01108	34.32	0.87	34.10
0.02802	22.77	1.07	22.54	0.01420	32.10	0.79	31.88
0.02141	24.44	0.89	24.23	0.01778	30.25	0.73	30.02
0.02937	22.60	0.60	22.36	0.02165	29.20	0.68	28.95
0.03886	20.53	0.48	20.26				
0.04984	18.46	0.43	18.17				

TABLE II (continued)

$-t$ [(GeV/c) ²]	$d\sigma/dt$ (uncorrected) [mb/(GeV/c) ²]	Error [mb/(GeV/c) ²]	$d\sigma/dt$ [mb/(GeV/c) ²]	$-t$ [(GeV/c) ²]	$d\sigma/dt$ (uncorrected) [mb/(GeV/c) ²]	Error [mb/(GeV/c) ²]	$d\sigma/dt$ [mb/(GeV/c) ²]
10.02* GeV/c π^+				16.02* GeV/c π^+			
0.02604	28.26	0.65	27.98	0.02118	27.05	1.81	26.82
0.03073	27.20	0.61	26.90	0.01581	29.83	1.57	29.62
0.03592	25.38	0.57	25.06	0.02165	26.59	1.01	26.37
0.04138	24.51	0.55	24.17	0.02845	24.70	0.80	24.44
0.04722	23.30	0.53	22.95	0.03638	22.54	0.71	22.26
0.05362	21.26	0.49	20.90	0.04544	22.01	0.67	21.68
0.06038	20.69	0.48	20.31	0.05557	19.31	0.61	18.98
0.06739	20.06	0.46	19.67	0.06657	17.63	0.56	17.29
				0.07867	16.11	0.53	15.76
11.95* GeV/c π^+				0.09182	14.74	0.50	14.39
0.00263	81.72	4.24	77.00	0.10600	12.29	0.44	11.97
0.00341	61.37	3.39	59.23	0.12087	11.89	0.44	11.55
0.00430	50.80	2.86	49.70	0.13680	10.44	0.40	10.13
0.00531	43.32	2.62	42.68	0.15405	9.22	0.37	8.92
0.00639	38.57	2.45	38.15	0.17186	8.37	0.35	8.08
0.00760	38.57	2.37	38.25				
0.00891	37.03	2.53	36.77	17.96 GeV/c π^+			
0.01029	35.19	2.71	34.95	0.00125	259.7	17.3	217.4
0.01179	35.66	3.13	35.43	0.00184	131.97	8.32	119.85
0.00876	39.89	2.66	39.62	0.00253	82.44	5.31	77.93
0.01202	32.88	1.66	32.67	0.00329	61.44	3.94	59.41
0.01584	29.10	1.30	28.89	0.00416	48.13	3.33	47.09
0.02028	31.47	1.20	31.22	0.00513	43.79	2.90	43.18
0.02531	26.95	1.10	26.69	0.00621	39.40	2.72	39.00
0.03089	23.33	1.01	23.07	0.00741	36.14	2.60	35.84
0.03709	23.98	0.94	23.68	0.00873	31.64	2.64	31.41
0.04378	22.09	0.87	21.77	0.01007	26.46	2.76	26.27
0.05101	20.81	0.84	20.48	0.01156	29.20	2.88	29.01
0.05887	20.63	0.81	20.26	0.01325	28.72	3.61	28.53
0.06728	18.23	0.76	17.88	0.01013	31.30	2.58	31.09
0.07617	17.26	0.74	16.90	0.01391	29.14	1.67	28.95
0.08580	15.44	0.67	15.09	0.01822	26.68	1.30	26.48
0.09580	15.29	0.69	14.92	0.02328	23.11	1.13	22.90
				0.02901	24.00	1.08	23.74
14.00 GeV/c π^+				0.03560	22.87	1.02	22.59
0.00111	332.7	18.3	270.6	0.04276	21.51	0.95	21.21
0.00152	171.4	10.1	149.5	0.05057	20.82	0.92	20.49
0.00199	119.19	6.94	110.00	0.05879	16.70	0.82	16.41
0.00252	88.20	5.44	83.74	0.06768	15.93	0.78	15.62
0.00311	73.33	4.56	70.98	0.07746	15.64	0.77	15.31
0.00377	57.13	3.95	55.79	0.08789	14.36	0.72	14.03
0.00449	51.80	3.83	50.95	0.09878	13.37	0.70	13.03
0.00526	37.26	3.46	36.70	0.11040	11.87	0.66	11.55
0.00611	42.77	4.03	42.35				
0.00704	39.96	3.90	39.64	20.19 GeV/c π^+			
0.00799	34.90	4.62	34.63	0.00102	418.0	39.7	333.8
0.00613	43.44	3.81	43.03	0.00161	163.1	15.0	144.1
0.00839	35.12	2.28	34.87	0.00230	88.98	8.24	82.90
0.01104	33.42	1.82	33.21	0.00318	61.38	5.62	59.10
0.01415	29.93	1.69	29.73	0.00417	54.18	4.35	53.12
0.01761	26.36	1.52	26.16	0.00525	42.62	4.17	42.04
0.02157	27.81	1.44	27.58	0.00647	32.08	3.55	31.73
0.02592	26.28	1.39	26.02	0.00790	39.11	3.14	38.83
0.03068	24.57	1.30	24.30	0.00936	37.22	3.15	36.98
0.03572	23.54	1.26	23.25	0.01101	28.32	3.31	28.12
0.04118	20.79	1.16	20.51	0.01273	26.09	3.35	25.91
0.04723	22.37	1.16	22.03	0.01465	24.41	3.57	24.24
0.05337	19.73	1.08	19.41	0.01660	28.24	3.79	28.03
0.06021	18.75	1.04	18.41	0.01103	28.19	3.47	28.00
0.06713	17.47	0.99	17.13	0.01757	27.78	1.93	27.57
				0.02235	26.61	1.54	26.38
16.02* GeV/c π^+				0.02953	20.57	1.35	20.35
0.00244	93.57	4.98	87.11	0.03666	21.35	1.17	21.08
0.00350	60.06	3.02	57.96	0.04499	18.98	1.17	18.70
0.00474	46.95	2.25	46.07	0.05385	18.46	1.08	18.16
0.00615	38.02	1.88	37.55	0.06391	16.74	1.03	16.43
0.00773	33.70	1.68	33.40	0.07435	15.37	0.96	15.05
0.00955	32.05	1.54	31.81	0.08559	13.87	0.92	13.55
0.01155	32.37	1.52	32.16	0.09782	12.22	0.90	11.92
0.01369	32.28	1.48	32.06	0.11100	12.51	0.83	12.18
0.01607	30.94	1.57	30.72	0.12484	10.25	0.76	9.96
0.01851	27.50	1.58	27.28	0.13919	9.13	0.72	8.85

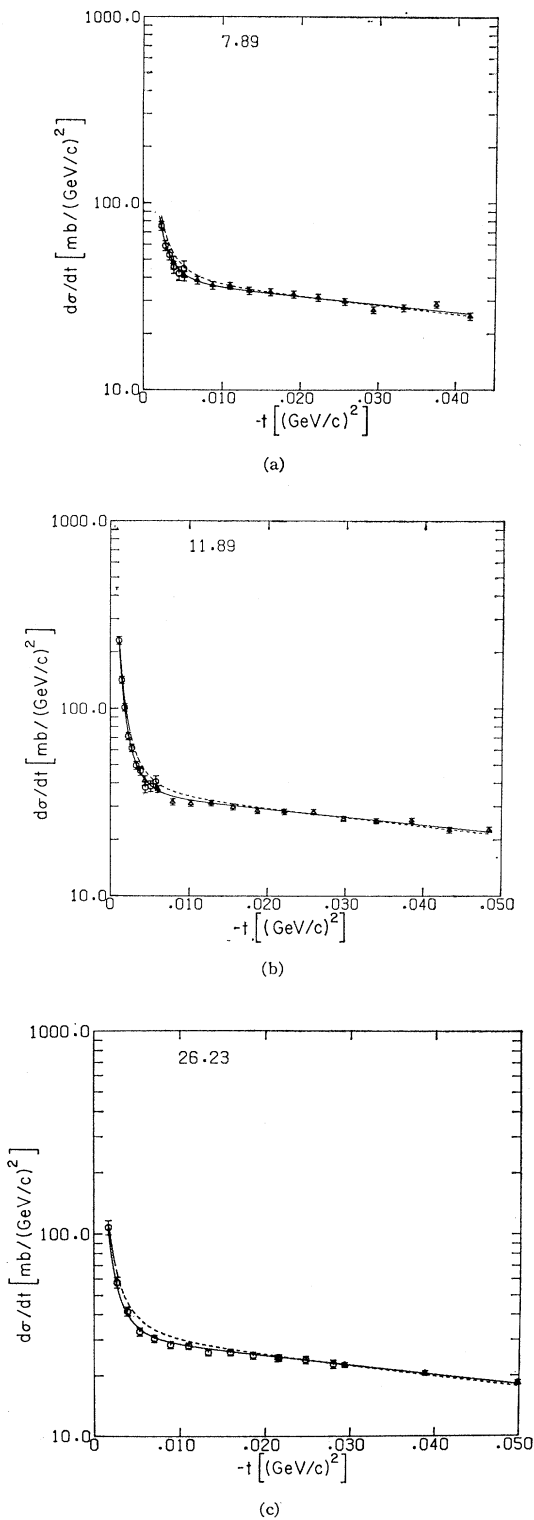


FIG. 4. Typical π^-p differential elastic-scattering cross sections at (a) 7.89, (b) 11.89, and (c) 26.23 GeV/c . The lines shown are the fits described in Sec. VI. As in the fit, a cutoff has been applied for $|t| > 0.05$ $(\text{GeV}/c)^2$.

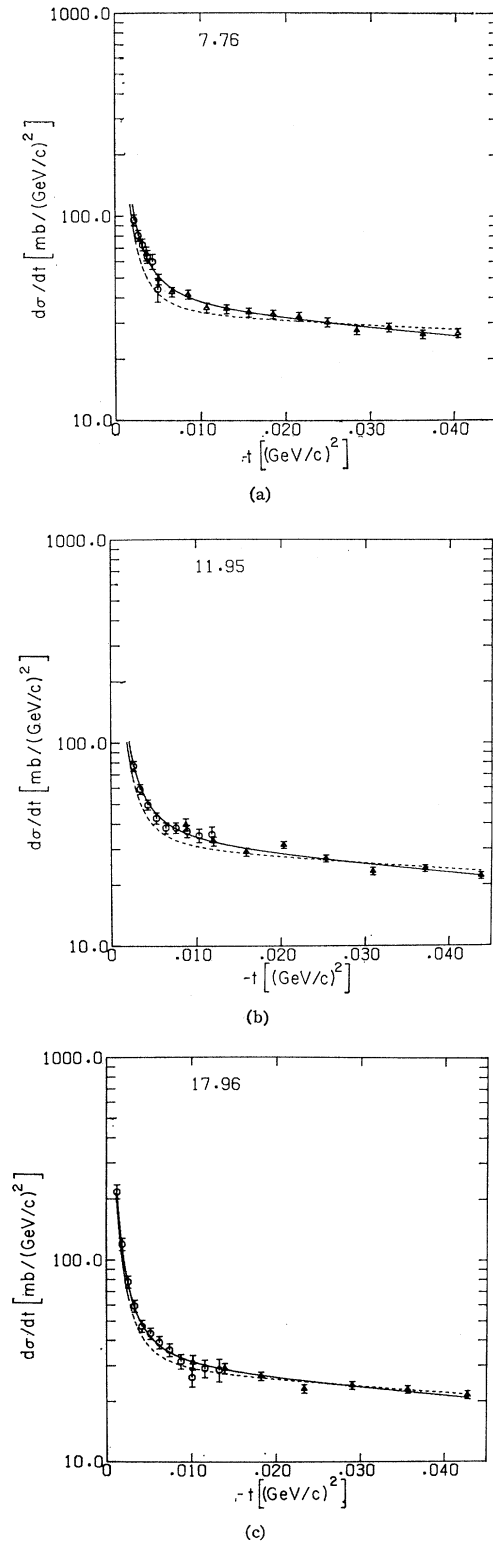


FIG. 5. Typical π^+p differential elastic-scattering cross sections at (a) 7.76, (b) 11.95, and (c) 17.96 GeV/c . The lines shown are the fits described in Sec. VI. As in the fit, a cutoff has been applied for $|t| > 0.05$ $(\text{GeV}/c)^2$.

marked with asterisks indicate runs taken with the second setup which covered a wider angular region. We have cut off the data with $|t| < 0.001$ (GeV/c)² in the first setup and for $|t| < 0.002$ (GeV/c)² in the second setup in order to keep uncertainties in the t values and in the multiple-scattering corrections small. The errors shown are the result of compounding statistical errors and the uncertainty due to the evaluation of t . At each momentum, a systematic scale uncertainty of $\pm 0.5\%$ must be applied, together with an additional 0.5% momentum-independent scale uncertainty.

VI. DEDUCTION OF THE REAL PART OF THE SCATTERING AMPLITUDE

A. Fitting Formula

The measured differential cross sections discussed above were fitted with a function involving a Coulomb term, a nuclear term, and a Coulomb-nuclear interference term. For pion-nucleon scattering, invariance principles limit the nuclear scattering amplitude to a form involving two complex functions of the energy and four-momentum transfer:

$$F_N(s,t) = f(s,t) + g(s,t)\boldsymbol{\sigma} \cdot \mathbf{n} \sin\theta, \quad (2)$$

where t is the negative square of the four-momentum transfer and s is the square of the total energy in the c.m. system. At small angles the Coulomb scattering amplitude is "non-spin-flip" in form, and so only the first term in F_N is involved in Coulomb-nuclear interference. Consequently, the spin-flip term appears in $d\sigma/dt = |F_N|^2$ only as the square of its amplitude and hence vanishes at small angles like $\sin^2\theta$. Since the scattering angles where the Coulomb-nuclear interference is large are $\lesssim 10$ mrad, we can safely neglect this term. We will use subscripts (+ or -) on $f(s,t)$ and α to denote the sign of the charge of the incident pion. The differential cross sections for π^+p and π^-p elastic scattering can then be written as follows:

$$(d\sigma/dt)(\pi^+p) = F_c^2/t^2 - (2F_c/|t|) \text{Im}f_+[\alpha_+ \cos 2\delta + \sin 2\delta] + (1 + \alpha_+^2)(\text{Im}f_+)^2, \quad (3)$$

$$(d\sigma/dt)(\pi^-p) = F_c^2/t^2 + (2F_c/|t|) \text{Im}f_-[\alpha_- \cos 2\delta - \sin 2\delta] + (1 + \alpha_-^2)(\text{Im}f_-)^2, \quad (4)$$

where $\alpha = \text{Re}f/\text{Im}f$ and $F_c = +[(2\sqrt{\pi})e^2/\beta c] \times$ (form factor). With our sign convention, the real part of the scattering amplitude is negative for a repulsive interaction.

The Coulomb form factor is the product of the form factors for the proton and the pion. Since there are no accurately measured values for the pion, we have used the proton form factor¹³ with the magnetic moment term removed; this approximation is reasonable since the near equality of the exponential slopes of the $\pi-p$

and $p-p$ differential cross sections indicate approximately equal radii of interaction. In any case, this term has little effect in the region of strong Coulomb-nuclear interference.

Some time ago Bethe¹⁴ used a nonrelativistic model to calculate δ , the relative phase introduced between the nuclear and Coulomb amplitudes by the long-range Coulomb force. He obtained $\delta = (e^2/\hbar c\beta) \ln(1.06/pa\theta)$, where a is the nuclear-radius parameter. In a number of recent papers,¹⁵ the calculation of δ has been investigated in some detail. Yennie and West treated the problem in detail on the fundamental basis of relativistic quantum electrodynamics and we have used their formula¹² in the data analysis:

$$2\delta = (e^2/\hbar c)[2 \ln(kb'\theta) + \gamma], \quad (5)$$

where $b' = (B^2 + r_\pi^2 + r_p^2)^{1/2}$, and B is deduced from the pion-nucleon elastic cross section by means of the formula $d\sigma/dt = e^{2A+2B^2t}$. γ is Euler's constant. From this and other papers^{14,15} we estimate the uncertainty in δ to be approximately equal to $\gamma e^2/2\hbar c$.

We have assumed that α is independent of t , which is a reasonable assumption in this range of t and, as will be seen later, fits the data very well. It is important to note that our data points extend to $|t| \sim 0.001$ (GeV/c)². This t is sufficiently close to zero that even if the shape of the real amplitude changes to e^{100t} below our region of measurement, our value of α would be wrong by only 10%. An exponential slope as large as 100 (GeV/c)⁻² corresponds to an interaction range $> 3F$, more than three times the value of the range of the pion-nucleon interaction deduced from other experiments. We have deduced $\text{Im}f$ at $t=0$ from the total cross section σ , using the optical theorem, $\text{Im}f(s,0) = \sigma(s)/4(\sqrt{\pi})\hbar$, and used for the dependence of f , the form that fits the larger $|t|$ measurements¹⁶:

$$|f(s,t)|^2 = |f(s,0)|^2 e^{bt+ct^2}. \quad (6)$$

In fitting the data, we fixed c at 2.4 (GeV/c)⁻⁴, the average value from larger $|t|$ measurements.¹⁶ The total cross section σ was obtained from measurements made from 8 to 22 GeV/c for π^+p and from 8 to 29 GeV/c for π^-p at 2 GeV/c intervals in a separate part of this experimental program.¹ In the fit to the differential cross section, the value of σ for each momentum was derived from parameters fitted to the measured total cross sections.

¹⁴ H. A. Bethe, Ann. Phys. (N. Y.) **3**, 190 (1958).

¹⁵ J. Rix and M. Thaler, Phys. Rev. **152**, 1357 (1966); M. M. Islam, *ibid.* **162**, 1426 (1967); M. P. Locher, Nucl. Phys. **B2**, 525 (1967); L. D. Soloviev, CERN Report No. 68-7, 1967 (unpublished); R. Serber (private communication).

¹⁶ K. J. Foley, S. J. Lindenbaum, W. A. Love, S. Ozaki, J. J. Russell, and L. C. L. Yuan, Phys. Rev. Letters **11**, 425 (1963); K. J. Foley, R. S. Gilmore, S. J. Lindenbaum, W. A. Love, S. Ozaki, E. H. Willen, R. Yamada, and L. C. L. Yuan, *ibid.* **15**, 45 (1965).

¹³ L. N. Hand, D. G. Miller, and R. Wilson, Rev. Mod. Phys. **35**, 335 (1963).

B. Results of the Fits

The method of least squares was used to fit the data with α and b as free parameters. By varying the range of t included in the fit, it was discovered that the error on α varied very little when the points at $|t| > 0.05$ (GeV/c)² were removed, which indicated that these points had little weight in determining the real part of the nuclear scattering amplitude. Since the parametrization is strictly empirical, and might, in fact, be incorrect over a wide t range, it was decided that points with $|t| > 0.05$ (GeV/c)² should not be used in the fit, in order that the particular form chosen for the nuclear amplitude should not bias the results. Table III gives the values of α and b , their errors¹⁷ and the χ^2 obtained together with the number of degrees of freedom. The starred momenta are those done with the second setup. The χ^2 distribution is reasonable, indicating that two parameters are adequate to fit the data. The solid lines on Figs. 4 and 5 are these fits to the data. The broken lines are best fits with α set equal to zero. In order to show more clearly the magnitude of the interference effect, we have subtracted the single Coulomb scattering from the data. The results are given in Figs. 6 and 7 and show very clearly the destructive interference for π^-p and constructive interference for π^+p scattering.

We also fitted the data allowing the zero-angle imaginary amplitude to be a free parameter instead of using the optical theorem to deduce it from the total cross section. The values of α obtained were usually

equal, within errors, to those given in Table III, but the error on α became a strong function of the t cutoff. In particular, the cross sections for $|t| > 0.05$ (GeV/c)² (i.e., outside the region of strong nuclear-Coulomb interference) had substantial weight in determining α , indicating that the deduction of α was no longer dependent only on the interference term. For this reason we do not consider this procedure to be as reliable as that described above.

C. Discussion of the Errors in α

The statistical errors in α given in Table III are those obtained from the least squares fit. In addition to these errors, several systematic errors must be applied. The largest is due to the uncertainty in the detection efficiency of the system. As discussed in Sec. IV, this uncertainty is $\pm 1\%$, about half of which is of a scale nature. The total cross sections were measured with a precision of $\pm 0.3\%$. Allowing the value of σ used to determine $\text{Im}f(s,0)$ at each momentum to vary by this amount introduces an average change of $\sim \pm 0.004$ in α . With the exception of the 0.5% scale uncertainty, the systematic errors described above are believed to be uncorrelated. Consequently, we have compounded them with the 0.2% error in $d\sigma/dt$ due to the uncertainty in the incident momentum to arrive at the systematic error shown for each momentum in Table III. We also give the error obtained by compounding the systematic and statistical errors which

TABLE III. Results of the two-parameter fit to the data of Table II with $|t| < 0.05$. The starred (*) momenta indicate measurements with the second (wide-angle) arrangement. The column labeled α is the ratio of real to the imaginary parts of scattering amplitudes. The column labeled $\Delta\alpha(\text{Stat})$ is the error propagated through the least squares fit (mostly statistical error). The column labeled $\Delta\alpha(\text{Sys})$ is the systematic error due to the estimated errors in the efficiency measurements, the total cross sections, and the incident momentum. These two errors are compounded in the next column. The slope parameter b and its error are given in columns 6 and 7. The last two columns compare the χ^2 obtained for the fit with the number of degrees of freedom (N.D.F.) of each measurement.

Momentum (GeV/c)	α	$\Delta\alpha(\text{Stat})$	$\Delta\alpha(\text{Sys})$	$[\Delta\alpha^2(\text{Stat}) + \Delta\alpha^2(\text{Sys})]^{1/2}$	$b/2$ (GeV/c) ⁻²	$\Delta b/2$ (GeV/c) ⁻²	χ^2	N.D.F.
7.89* π^-	-0.123	0.025	0.008	0.026	5.24	0.24	10	18
9.84 π^-	-0.128	0.018	0.007	0.019	5.17	0.30	23	20
9.89* π^-	-0.157	0.023	0.008	0.024	5.39	0.20	11	17
11.89 π^-	-0.122	0.016	0.008	0.018	5.17	0.17	16	22
14.16 π^-	-0.113	0.024	0.008	0.025	4.98	0.25	11	20
15.99 π^-	-0.127	0.018	0.008	0.019	5.49	0.16	10	19
16.00* π^-	-0.154	0.023	0.009	0.025	5.62	0.16	17	14
18.19* π^-	-0.113	0.025	0.009	0.027	5.04	0.15	10	14
20.15 π^-	-0.100	0.024	0.009	0.026	5.44	0.21	8	17
20.38 π^-	-0.119	0.017	0.009	0.019	5.63	0.13	14	17
22.13 π^-	-0.111	0.025	0.009	0.027	5.43	0.20	10	16
24.22 π^-	-0.123	0.027	0.009	0.029	5.44	0.21	7	15
26.23 π^-	-0.139	0.028	0.009	0.029	5.80	0.15	5	15
7.76* π^+	-0.212	0.022	0.007	0.023	4.17	0.40	8	18
9.86 π^+	-0.221	0.020	0.008	0.022	4.19	0.51	23	20
10.02* π^+	-0.201	0.011	0.008	0.014	4.23	0.17	18	17
11.95* π^+	-0.187	0.022	0.009	0.024	4.60	0.35	16	15
14.00 π^+	-0.190	0.022	0.008	0.023	4.67	0.38	15	20
16.02* π^+	-0.170	0.021	0.008	0.022	4.28	0.29	11	14
17.96 π^+	-0.143	0.025	0.008	0.026	4.62	0.40	10	17
20.19 π^+	-0.180	0.035	0.008	0.036	5.51	0.53	17	17

¹⁷ The errors quoted are the square roots of the diagonal elements of the error matrix. No adjustment has been made on the basis of the χ^2 for the fit.

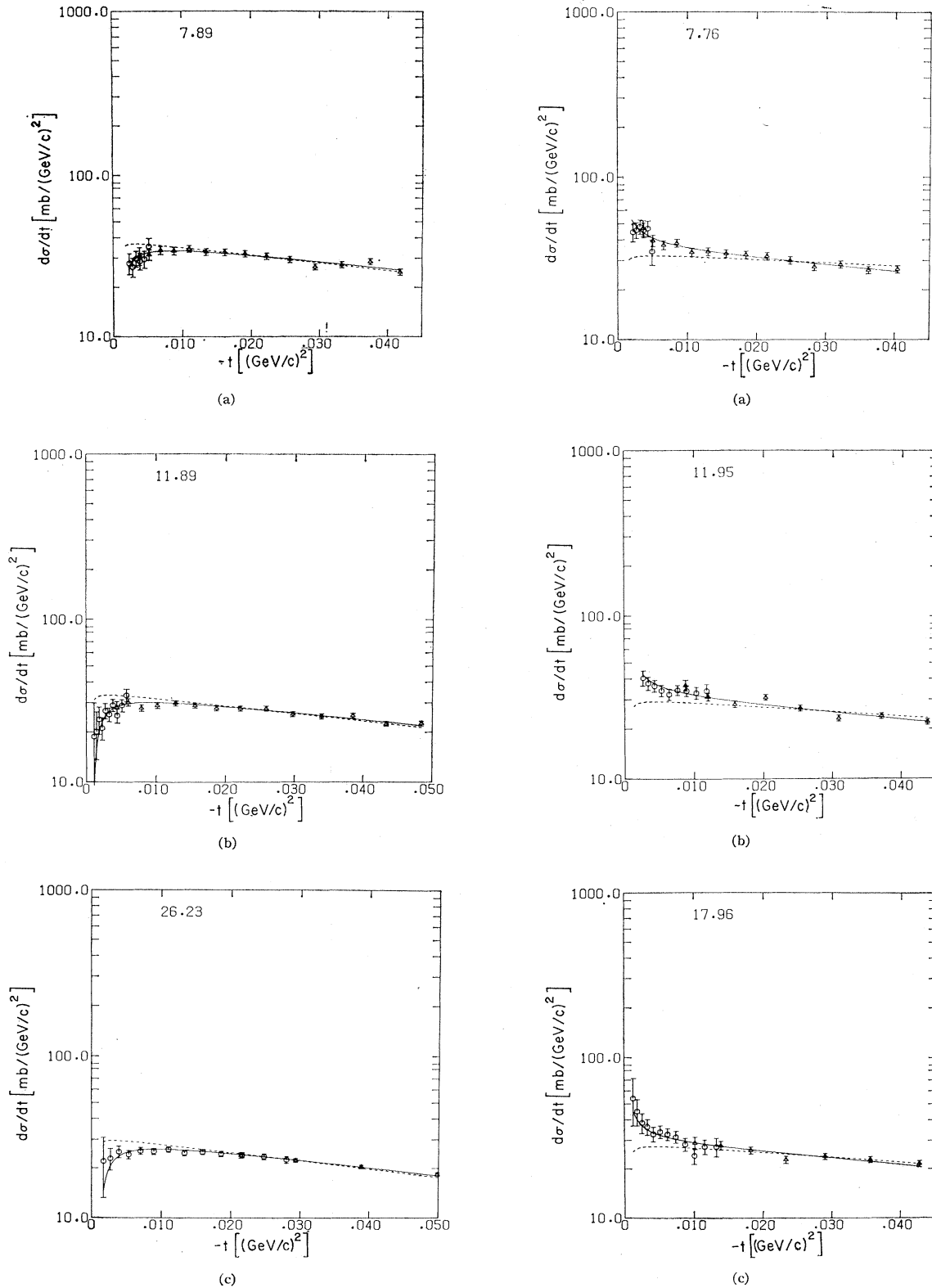


FIG. 6. Values of the π^-p differential cross sections at (a) 7.89 (b) 11.89, and (c) 26.23 GeV/c after subtraction of single Coulomb scattering. The destructive interference is very apparent.

FIG. 7. Values of the π^+p differential cross sections at (a) 7.76, (b) 11.95, and (c) 17.96 GeV/c, after subtraction of single Coulomb scattering. The constructive interference is very apparent.

we shall use as the over-all point-to-point error on α . The 0.5% scale uncertainty produces an additional uncertainty of ± 0.006 .

One error not included in the above is the uncertainty in the Coulomb phase δ . As discussed earlier, we estimate the error in δ to be of the order of $\pm \gamma e^2/2\hbar c$. This produces an uncertainty of ± 0.007 in α . However, we have not included this in the errors shown in Table III since presumably it can eventually be reduced by more accurate calculations. New values of α can then be deduced.

D. Correlation of Systematic Error in α^\pm

An important feature of the above sources of systematic error is that each is of such a nature as to shift the π^- and π^+ differential cross sections in the same direction. This is obviously true of any error in the multiple Coulomb-scattering corrections and in δ . It is also true of the efficiency uncertainty, which should be independent of the sign of the charge of the particle at any one momentum. Because the Coulomb-nuclear interference is of opposite sign in π^-p and π^+p scattering, any error which tends to shift the differential cross section in the same direction will tend to cancel when the sum of α^- and α^+ is considered. On the other hand, the difference between α^- and α^+ has large systematic errors.

VII. COMPARISON OF $\pi^\pm p$ RESULTS WITH DISPERSION RELATIONS

A. Evaluation of the Forward Dispersion Relations

Since the original derivation of the charged pion-nucleon forward dispersion relations and subsequent rigorous proofs,¹⁸ it has become increasingly clear that they represent the most quantitative experimental checks of the basic axioms of a local relativistic field theory. The assumptions of unitarity, relativistic invariance, local commutativity (i.e., microscopic causality) and certain reasonable mass spectra can be used to prove the analyticity of the scattering amplitude

TABLE IV. Parameters of the three total cross-section fits used to perform the high-energy part of the dispersion integrals. Evaluation of the fits yields the total cross sections in millibarns, where p is the lab momentum in GeV/c.

Fit	$\sigma = A + B/p^C$	A	B	C
I	σ_{π^+}	22.598	25.936	1.057
	σ_{π^-}	22.598	19.605	0.669
II	$\sigma_{\pi^-} + \sigma_{\pi^+}$	44.238	36.96	0.694
	$\sigma_{\pi^-} - \sigma_{\pi^+}$	0	3.847	0.306
III	$\sigma_3 = \sigma_{\pi^+}$	22.522	24.822	1.023
	σ_1	22.522	19.861	0.580

¹⁸ M. L. Goldberger, Phys. Rev. **99**, 979 (1955); M. L. Goldberger, H. Miyazawa, and R. Oehme, *ibid.* **99**, 986 (1955); K. Zyzanski, *ibid.* **105**, 743 (1957); N. N. Bogolubov and V. S. Vladimirov, Izv. Akad. Nauk. USSR Ser. Mat **22**, 15 (1958).

necessary for the use of the Cauchy theorem to deduce the forward dispersion relations.

In order to compare the experimental results with the theoretical predictions, we have evaluated the $\pi^\pm p$ forward dispersion relations in the following well-known form:

$$D_i^+(\omega) = D_i^+(1) + \frac{f^2 k^2}{M[1 - (1/2M)^2][\omega^2 - (1/2M)^2]} + \frac{k^2}{4\pi^2} P \int_1^\infty \frac{\omega' (\sigma_- + \sigma_+)}{k' (\omega'^2 - \omega^2)} d\omega', \quad (7)$$

$$D_i^-(\omega) = \frac{2f^2 \omega}{\omega^2 - (1/2M)^2} + \frac{\omega}{4\pi^2} P \int_1^\infty \frac{k'}{\omega'^2 - \omega^2} \times (\sigma_- - \sigma_+) d\omega', \quad (8)$$

where D_+ and D_- , the real parts of the scattering amplitudes for cases π^+p and π^-p , respectively, are given by

$$D_i^+ = \frac{1}{2}(D_+ + D_-), \quad (9)$$

$$D_i^- = (D_- - D_+). \quad (10)$$

We have set $f^2 = 0.081$ and $D_i^+(1) = -0.002$.⁴ All of the amplitudes above are in natural units ($\hbar = c = m_\pi = 1$) in the lab system, the square of the scattering amplitude giving $d\sigma/d\Omega$.

In Eq. (7), the singly-subtracted dispersion-relation integral for D_i^+ will be convergent if $(\sigma^+ + \sigma^-)/\omega$ converges at high energy. In Eq. (8), the unsubtracted dispersion-relation integral for D_i^- converges if $\sigma_- - \sigma_+ \rightarrow 0$ faster than $1/\ln\omega$. The evidence obtained in total-cross-section measurements is consistent with the above requirements, and, in the case of D_i^+ , the limit of the Froissart bound,¹⁹ $\sigma_{\text{tot}} < \text{const} \ln^2 \omega$, also gives convergence.

The dispersion-relation integrals were evaluated as follows: Up to 5 GeV/c, consecutive linear approximations were made to the measured total cross sections over small energy regions which were chosen such that the linear approximations fitted the data well. The integrals were then performed with no further approximations. In the next region up to 1800 GeV/c, fits to the cross-section data above 5 GeV/c were used instead of data points.¹ Above 1800 GeV/c, the integrals were evaluated using the fits and an expansion of the integral for $\omega' \gg \omega$. The three fits used are given in Table IV. Each fit assumed that the difference $(\sigma_- - \sigma_+)$ approached zero as the momentum increased and that the momentum dependence of each of two independent combinations could be fitted with two parameters. The first fit (I) used the π^+p and π^-p cross sections themselves, the second fit (II) used the sum and the difference $\sigma_- \pm \sigma_+$, and the third fit (III) used the $T = \frac{1}{2}$ and $T = \frac{3}{2}$ cross sections.

¹⁹ M. Froissart, Phys. Rev. **123**, 1053 (1961); A. Martin, Nuovo Cimento **42A**, 930 (1966); **44A**, 1219 (1966).

B. Comparison of the Data with the Dispersion-Relation Predictions

The values of α_{\pm} deduced in this experiment are shown in Fig. 8. The solid line is the result for the dispersion-relation integral using fit I. The dashed line shows the effect of displacing the curve for the fit by the estimated systematic scale error on the data which was obtained by adding the contributions from the 0.5% scale uncertainty on the differential cross sections and the uncertainty in δ . The two contributions were ± 0.006 and ± 0.007 , respectively. Considering the errors, the agreement is good.

Figure 9 shows the calculations and the data for D^+ from 8–20 GeV/c in the c.m. system in natural units, $\hbar=c=m_{\pi}=1$. These data points were obtained by using the measurements of α_{\pm} at nearby momenta and have been plotted at the mean momentum. As discussed previously, the systematic errors are such as to nearly cancel in considering D^+ and, hence, the residual systematic error is small compared with the statistical errors already assigned to the points. In order to assess the effect on D^{\pm} of the uncertainty in the low-energy total cross sections, we depressed the $\pi+p$ total cross sections in the region 2–6 GeV/c by subtracting a Breit-Wigner bump 2% in height centered at 4 GeV/c and with $\Gamma=1$ GeV. This produced a change in D^+ amounting to 0.002 at 10 GeV falling to 0.0015 at 20 GeV. The change in D^- was 0.001 at 10 GeV falling to 0.0004 at 20 GeV/c. Even depressing both total cross sections by 2% for all energies below 4 GeV, tapering the perturbation to zero at 6 GeV, changed D^+ by 0.015 at 10 GeV, 0.01 at 20 GeV. The uncertainties in f^2 and $D^+(1)$ cause negligible errors in D^+ and D^- . The solid curves in Fig. 9 used fits I, II, and III, as indicated. As can be seen, the agreement is excellent in all three cases, demonstrating the validity of the $\pi^{\pm}-p$ forward dispersion relation for D^+ , provided that the

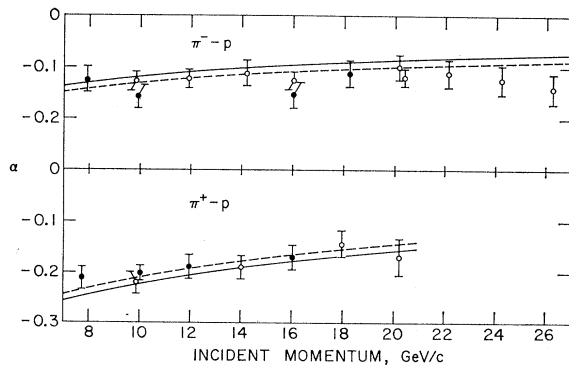


FIG. 8. Experimental values of $\alpha = \text{Re } f / \text{Im } f$. The solid lines are the results of the dispersion-relation fits. The dashed line is the result of shifting the dispersion-relation results by the additional systematic scale error to be applied to α . As is discussed in the text, this error is such as to move α_+ and α_- in opposite directions.

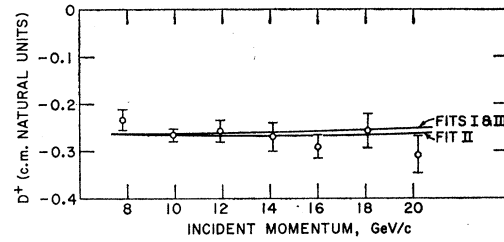


FIG. 9. Values of D^+ in natural units in the c.m. system. The curves are the results of the dispersion-relation integrals discussed in Sec. VII B.

extrapolated asymptotic behavior of the total cross sections is correct.

In order to make the test virtually independent of the behavior of the total cross sections at higher energies where no measurements have been made, an additional subtraction has been performed on D^+ at 20 GeV. This results in the solid line on Fig. 10, which is an excellent fit to the data. In order to show that the resultant D^+ (doubly subtracted) dispersion relation is very insensitive even to drastic and physically unjustified assumptions about the behavior of the total cross section at high energies, we have calculated D^+ for the following two cases:

(1) We force both the π^++p and the π^-+p total cross sections to drop suddenly to zero at 35 GeV/c and remain zero at all higher energies. The resulting prediction for D^+ is shown by the dotted line in Fig. 10.

(2) We let both the π^++p and the π^-+p total cross sections increase somewhat faster than linearly ($\sigma \propto p^{1.1}$) with increasing energy above 35 GeV/c. The resulting prediction for D^+ is shown by the dashed line in Fig. 10. As we can see, even these drastic assumptions cause only small changes in the predicted magnitude of D^+ . Hence, we can safely conclude that any reasonable variations in the asymptotic behavior of the total cross sections will not affect the agreement of the data with the doubly subtracted D^+ forward dispersion relation.

Figure 11 shows the calculated results for D^- for fits I, II, and III compared with the data from 8–20 GeV/c. As pointed out previously, the systematic errors tend to add in D^- . Consequently, in calculating

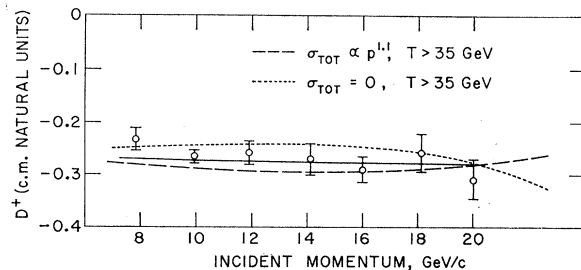


FIG. 10. Values of D^+ in c.m. natural units. The curves are the results obtained from the doubly subtracted dispersion-relation integral using the assumed total cross-section behaviors discussed in Sec. VII B.

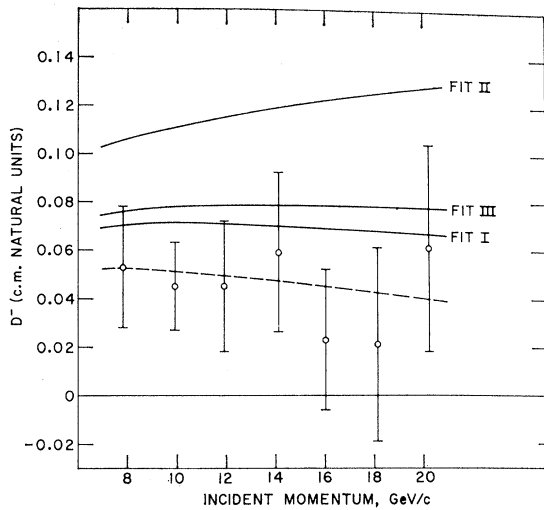


FIG. 11. Values of D^- in c.m. natural units. The curves are the results of the dispersion-relation integrals discussed in the text.

the errors on D^- , the two systematic errors propagated from α_+ and α_- were *added* before compounding with the two statistical errors. An additional systematic error comes from the over-all scale uncertainty of the experiment and the uncertainty in δ . This error, which is highly correlated and moves all points in the same direction, is indicated by the dashed line which results from displacing the results of fit I downward by this error. The data agree with fits I and III within the errors. However, fit II departs from the data by 2–3 standard deviations. In order for the functional form $\sigma_- - \sigma_+ \propto 1/p^n$ to fit D^- , the quantity n cannot be smaller than 0.4. We also note that in order to fit the total-cross-section data up to 22 GeV/ c with this form, we must have $n < 0.5$.

C. Question of a Fundamental Length

The dispersion relations that we have employed have been derived on the assumption that microscopic causality holds down to infinitesimal distances. There is no rigorous and well-defined way to incorporate a fundamental length in the theory, but several models have been investigated. Some time ago, Oehme²⁰ used a model in which, if causality fails for distances less than l , the forward dispersion relations break down completely at an energy $\omega \sim 1/l$. Using the agreement of our data with the doubly subtracted dispersion relation for D^+ , we see that $l \lesssim 10^{-15}$ cm. Since we have shown that the doubly subtracted dispersion relation is valid, virtually independent of the behavior of the total cross sections beyond the region presently available to experiments, this limit on the fundamental length is also independent of the high-energy behavior.

²⁰ R. Oehme, Phys. Rev. **100**, 1503 (1955).

It is possible that the agreement of the singly subtracted dispersion relation for D^+ with the data comes from chance cancellation of the effects of a fundamental length and the results of peculiar high-energy total-cross-section behavior, different from that obtained in the fits to the data. However, if we assume that this is not the case, then more stringent limits can be placed on l . One model is that of Oehme.²⁰ A relation quite similar to his Eq. (42) can be written for D^+ . Large deviations in D^+ are predicted at 20 GeV/ c even for a fundamental length of about 10^{-16} cm. Unfortunately, this type of relation together with analyticity requirements also predicts oscillation of total cross sections at high energy. A treatment which attempts to circumvent this difficulty is that of Blokhintsev.²¹ This work considered further the difficulty that in the theory of relativity a small spacelike separation can correspond to a large three-dimensional distance. In order to use his Eq. (12), we must extrapolate the dispersion-relation integral to an energy $1/l$; we have used fit I for this purpose. This treatment gives $l \lesssim 5 \times 10^{-16}$ cm.

VIII. TEST OF CHARGE INDEPENDENCE

So far we have not used the hypothesis of charge independence. If we make the assumption of charge independence of strong interactions, we can use our data to predict the charge-exchange cross section at $t=0$ via the relation

$$\left. \frac{d\sigma(\text{Ch. Ex.})}{dt} \right|_{t=0} = \frac{1}{2} [(\text{Re}f_- - \text{Re}f_+)^2 + (\text{Im}f_- - \text{Im}f_+)^2]. \quad (11)$$

There have been several measurements of the angular distribution for charge-exchange scattering in our energy region.²² The values obtained by the authors in extrapolating to $t=0$ are shown in Fig. 12 together with the predictions of Eq. (11). Considering the errors, the agreement is satisfactory, particularly when one notes that no error has been included for the uncertainty in the functional form to be used in extrapolating the charge-exchange data to $t=0$. One should note that even though the check is only to an accuracy of 10%–20% of the charge-exchange amplitude, this amplitude is itself less than 10% of the individual $T=\frac{3}{2}$ and $T=\frac{1}{2}$ amplitudes. Hence, any charge-dependent term in either of the individual amplitudes is limited to 1–2% of the amplitude.

²¹ D. I. Blokhintsev, Usp. Fiz. Nauk. **89**, 185 (1966) [English transl.: Soviet Phys.—Usp. **9**, 405 (1966)].

²² I. Mannelli, A. Bigi, R. Carrara, M. Wahlig, and L. Sodickson, Phys. Rev. Letters **14**, 408 (1965); A. V. Stirling, P. Sonderegger, J. Kirz, P. Falk-Vairant, O. Guisan, C. Bruneton, P. Borgeaud, M. Yvert, J. P. Guillaud, C. Caverzasio, and B. Amblard, *ibid.* **14**, 763 (1965).

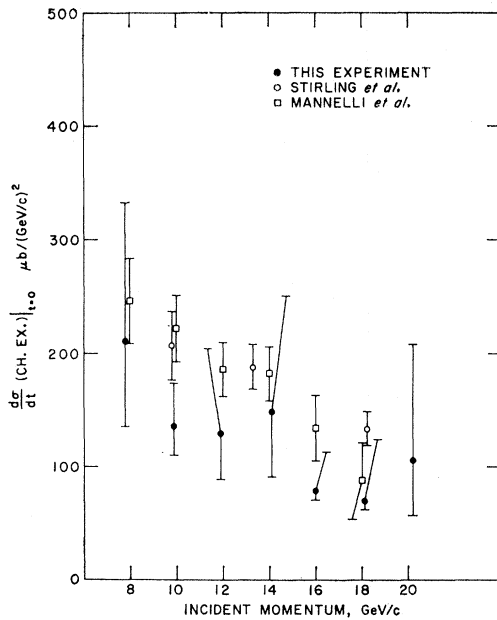


FIG. 12. Comparison of the charge-exchange cross section at $t=0$ and the values deduced from this experiment with the assumption of charge independence.

IX. CONCLUSIONS

The real part of the pion-proton scattering amplitude has been measured and compared with the predictions of the forward dispersion relations. The experiment critically verified the doubly subtracted D^+ dispersion relation up to 20 GeV/c incident momentum, virtually independent of assumptions about the high-energy

asymptotic behavior of the total cross sections. Even the singly subtracted D^+ dispersion relation is in excellent agreement with the data when simple inverse power-law fits are used to extrapolate the total cross sections. The predictions of the unsubtracted D^- dispersion relation are consistent with the experimental data within the error. This consistency strongly supports the validity of the Pomeranchuk theorem since the unsubtracted D^- dispersion integral would diverge if this theorem were violated.

Since the derivation of the forward dispersion relations depends on the analytic properties of the forward-scattering amplitude, unitarity, and crossing symmetry, the excellent agreement of the data with the theoretical predictions indicates that, at least up to the present energies, these basic assumptions are valid. One of the basic axioms required for derivation of the analytic properties is that of microscopic causality. Using the models described in Sec. VII C, we have derived that any acausal region characterized by a fundamental length is smaller than 10^{-15} cm, and probably $\lesssim 10^{-16}$ cm.

ACKNOWLEDGMENTS

The assistance of the AGS Operations and Experimental Support groups is gratefully acknowledged. We also wish to thank the Cryogenics group for hydrogen targets and the High Energy Electronic Equipment Pool. The services of the staff of the On-Line Data Facility was essential to the success of the experiment. We also acknowledge the untiring efforts of our group technicians.